

## Morphology and kinematics of the gas envelope of the Mira binary W Aquilae <sup>\*</sup>

D. T. Hoai, P. T. Nhung, P. N. Diep, N. T. Phuong, P. Tuan-Anh, N. T. Thao and P. Darriulat

Department of Astrophysics, Vietnam National Satellite Center, VAST, 18 Hoang Quoc Viet, Cau Giay, Hanoi, Vietnam; [dthoai@vnsc.org.vn](mailto:dthoai@vnsc.org.vn)

**Abstract** We analyse ALMA observations of the  $^{12}\text{CO}(3-2)$  emission of the circumstellar envelope (CSE) of the Mira variable binary star W Aql. These provide, for the first time, spatially resolved Doppler velocity spectra of the CSE up to angular distances to the central star of  $\sim 5''$  (meaning some 2000 AU). The exploratory nature of the observations (only five minutes in each of two different configurations) does not allow for a detailed modelling of the properties of the CSE but provides important qualitative information on its morphology and kinematics. Emission is found to be enhanced along an axis moving from east/west to north-east/south-west when the angular distance from the central star projected on the plane of the sky increases from zero to four arcseconds. In parallel, the Doppler velocity distribution displays asymmetry along an axis moving from east/west to north-west/south-east. The results are discussed in the context of earlier observations, in particular of the dust morphology.

**Key words:** stars: AGB and post-AGB – (*Star:*) circumstellar matter – Star: individual (W Aql) – Stars: mass-loss – radio lines: stars.

### 1 INTRODUCTION

W Aql is a Mira variable star of spectral type S6,6, namely in the transition between being oxygen and carbon dominated, with a period of 490 days, a mean luminosity of  $\sim 7000$  solar luminosities and an effective temperature of  $\sim 2000$  K (Sloan & Price 1998, Kukarkin et al. 1971, Feast & Whitelock 2000, Alfonso-Garzón et al. 2012, Ramstedt et al. 2009, Danilovich et al. 2014).

It is one of the few AGB stars for which direct evidence for the presence of a companion has been obtained (Ramstedt et al. 2011). A high-resolution Hubble Space Telescope<sup>1</sup> B-band image taken in 2004 at 435 nm (Figure 1) displays a clearly resolved binary system, the companion being located in the south-west direction at about  $56^\circ$  from west and at a projected distance of  $\sim 0.47''$  from the central star. The companion is a main sequence star with an effective temperature of  $\sim 6000$  K and a mass of  $\sim 1 M_\odot$  (Danilovich et al. 2015, Mayer et al. 2013). The distance from Earth is poorly known, with values between 230 pc and 610 pc being quoted in the literature (Guandalini & Busso 2008, Wallerstein et al. 2011, Knapp et al. 1998, Loup et al. 1993, Keenan & Boeshaar 1980, Danilovich et al. 2014, Ramstedt

---

<sup>\*</sup> This paper makes use of the following ALMA data: ADS/JAO.ALMA#<2012.1.00524.S>. ALMA is a partnership of ESO (representing its member states), NSF (USA) and NINS (Japan), together with NRC (Canada) and NSC and ASIAA (Taiwan), and KASI (Republic of Korea), in cooperation with the Republic of Chile. The Joint ALMA Observatory is operated by ESO, AUI/NRAO and NAOJ. The data are retrieved from the JVO portal (<http://jvo.nao.ac.jp/portal>) operated by the NAOJ

<sup>1</sup> Based on observations made with the NASA/ESA Hubble Space Telescope, obtained at the data archive at the Space Telescope Science Institute. STScI is operated by the Association of Universities for Research in Astronomy, Inc. under NASA contract NAS 5-26555.

et al. 2009, 2011, Ramstedt & Oloffson 2014), indirectly obtained from the luminosity-period relation (Whitelock et al. 1994, 2008). Retaining a distance of  $\sim 400$  pc, the projected distance between the central star and its companion is of the order of  $\sim 200$  AU. The real distance may be much larger as nothing is known of the inclination of the orbital plane on the sky. As two HST images separated by 11 years do not reveal any displacement between star and companion, the orbital period is estimated to exceed  $\sim 1000$  years (Mayer et al. 2013, Danilovich et al. 2015).

The star has been extensively observed in the visible, the infrared, down to far infrared, and radio. Ramstedt et al. (2011) have recently detected polarized light in the visible, namely essentially light from the star scattered from the dust in its CSE. As polarization is strongly peaked about  $90^\circ$  scattering, they observe the circumstellar dust in a slice containing the central star and parallel to the sky plane. Their observations reveal a clear enhancement of the emission in the south-west direction up to an angular distance of some  $10''$  from the central star. Close to the star, up to a distance of  $\sim 1''$ , the emission is clearly elongated around the north-east/south-west direction. While this direction corresponds to the line joining the central star to its companion in Figure 1, a causal relation between the two directions is far from obvious as the inclination of the orbit on the sky plane is unknown. The dust mass of the south-west feature is estimated to be (assuming optically thin dust-scattering) of the order of  $10^{-6} M_\odot$ .

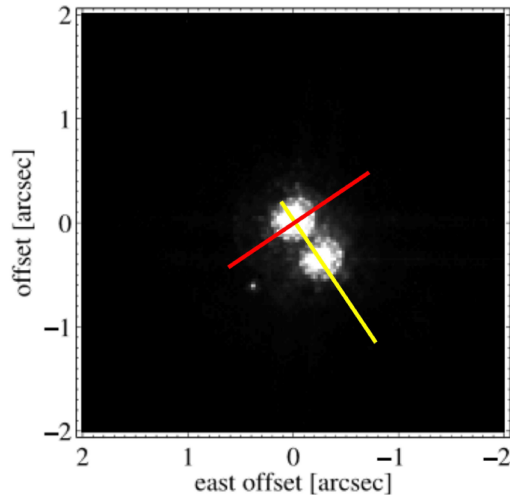


**Fig. 1** High-resolution HST B-band image of W Aql. The binary system is clearly resolved and the AGB star is centred. North is up and east is left. The yellow line, joining the central star to its companion, is at  $56^\circ$  clockwise from east/west, the red line at  $34^\circ$  counter-clockwise.

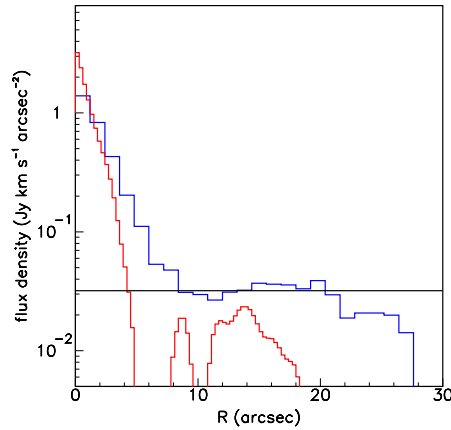
Radio single dish observations in the millimetre/sub-millimetre range include several molecular lines (Nyman et al. 1992, Knapp et al. 1998, Ramstedt et al. 2009, Wallerstein et al. 2011 and Ramstedt & Oloffson 2014). The associated line profiles cover typically a  $\pm 20$  km s $^{-1}$  Doppler velocity interval, giving evidence for significant winds. Danilovich et al. (2015) have recently modelled the line profiles of  $^{12}\text{CO}$ ,  $^{13}\text{CO}$ , SiO, H $_2$ O, HCN and NH $_3$ , and obtained a mass loss rate of  $4.0 \cdot 10^{-6} M_\odot \text{ yr}^{-1}$ , of the same order of magnitude as previous estimates that range between  $2.2 \cdot 10^{-6}$  and  $9.4 \cdot 10^{-6} M_\odot \text{ yr}^{-1}$  (Knapp et al. 1998, Ramstedt et al. 2009, De Beck et al. 2010). The profiles are approximately symmetric with an occasional slight excess emission on the blue-shifted side, suggesting an asymmetric outflow. Continuum emission has also been observed and the dust properties have been studied up to large distances from the central star (Mayer et al. 2013). The only interferometer observations that have been made are from the Berkeley Infrared Spatial Interferometer (ISI) at  $11 \mu\text{m}$  and

the Plateau de Bure Interferometer on CO molecular lines. The former use crude interferometry from three aligned antennae and find an excess of emission in the eastern half-plane for small distances from the central star, reaching to  $0.5''$  (Tatebe et al. 2006); the latter are part of the COSAS programme (Castro-Carrizo et al. 2010) but have not been published yet.

Recently, ALMA observations of the CO(3-2) emission of the circumstellar envelope have been made publicly available (ALMA 0100334[3/5]). The present work presents an analysis of these data, which provide for the first time spatially resolved Doppler velocity spectra.

## 2 OBSERVATIONS, DATA REDUCTION AND DATA SELECTION

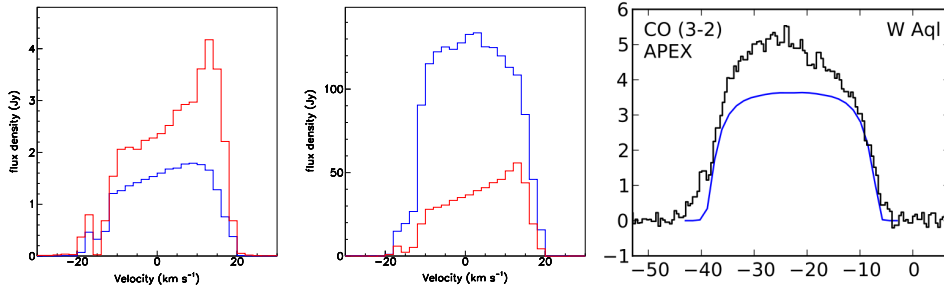
Two sets of observations were made on March 6<sup>th</sup> and 20<sup>th</sup>, 2014, each of five minutes duration, one with the normal array (ALMA) and the other with the compact array (ACA) with configurations giving beams of respective angular dimensions of  $1.1'' \times 1.0''$  and  $4.9'' \times 2.6''$  and position angles of  $-77.6^\circ$  and  $75.6^\circ$ . The line Doppler velocity spectra, are available in each case in bins of  $2 \text{ km s}^{-1}$  between  $-55.5 \text{ km s}^{-1}$  and  $4.5 \text{ km s}^{-1}$ . In what follows, we define the middle of the range,  $-25.5 \text{ km s}^{-1}$ , as origin of velocity coordinates. Also available are continuum flux densities averaged over a 15.8 GHz interval. The data have been reduced by the ALMA staff to clean maps using pixel sizes of  $0.1'' \times 0.1''$  (ALMA) and  $0.8'' \times 0.8''$  (ACA) respectively. We use orthonormal coordinates with  $x$  along the line of sight away from Earth,  $y$  pointing east and  $z$  pointing north.



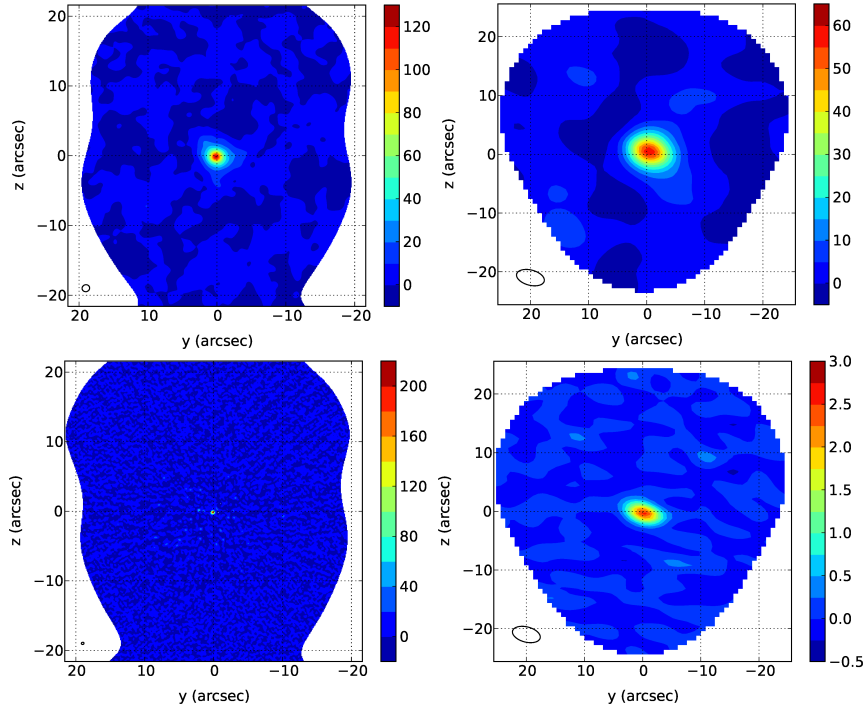
**Fig. 2** Distributions of the line flux integrated over Doppler velocities and averaged over position angles  $\varphi$  as a function of  $R = \sqrt{y^2 + z^2}$  for ALMA data (red) and ACA data (blue). The black line is for a flux of  $32 \text{ mJy km s}^{-1} \text{ arcsec}^{-2}$ .

Figure 2 shows the distributions of the line flux integrated over Doppler velocities and averaged over position angle  $\varphi = \tan^{-1}(\frac{z}{y}) + \pi$  ( $= 0$  west and positive clockwise) as a function of  $R = \sqrt{y^2 + z^2}$ , the projected angular distance from the star. It gives evidence at  $\sim 4''$  for a short spacing cut-off in the ALMA data, namely the flux filtered out by the interferometer, and for extended emission in the ACA data extending up to at least  $22''$  at a typical level of  $\sim 32 \text{ mJy km s}^{-1} \text{ arcsec}^{-2}$  (a constant level in  $R$  means a  $1/r$  dependence in space). Accordingly, in what follows, we restrict the analysis of the ALMA data to angular distances from the central star not exceeding  $4''$  (meaning  $\sim 1600 \text{ AU}$  in projected distance).

Figure 3 displays the dependence of the line flux density on Doppler velocity averaged over the central  $1.6'' \times 1.6''$  (left panel) and over a Gaussian circular beam having a FWHM of  $18''$  (central



**Fig. 3** Dependence of the line flux density on Doppler velocity averaged over the central  $1.6'' \times 1.6''$  (left panel) and integrated over a Gaussian beam of  $18''$  FWHM (central panel) for ALMA (red) and ACA (blue) data. The right panel shows the profile measured by Ramstedt et al. (2009) together with the model fit of Danilovich et al. (2015).



**Fig. 4** Sky maps of the detected fluxes for the line (upper panels) and the continuum (lower panels) and for ALMA data (left panels) and ACA data (right panels) separately. The beam is shown in the lower left corner. The color scales are in units of  $\text{Jy km s}^{-1} \text{arcsec}^{-2}$  for the line and  $\text{mJy arcsec}^{-2}$  for the continuum.

panel). The latter corresponds to the APEX single dish observation of Ramstedt et al. (2009) which is also displayed in the figure (right panel). Significant differences between the ALMA and ACA data are

the effect of the important short spacing problem in the former. In particular, the data integrated over the large Gaussian beam show directly that more than half of the total flux is contributed by the large distance environment of the star, at distances exceeding  $4''$ . While the line profile observed by ACA is in good agreement with that observed in the single dish APEX data, evidence for an important slope in the central region is obtained, the red-shifted side being enhanced with respect to the blue-shifted side by  $\sim 2\%$  per  $\text{km s}^{-1}$ . The slope is also apparent in the ACA data when they are restricted to the central region (here a square of  $1.6'' \times 1.6''$ , significantly smaller than the beam size).

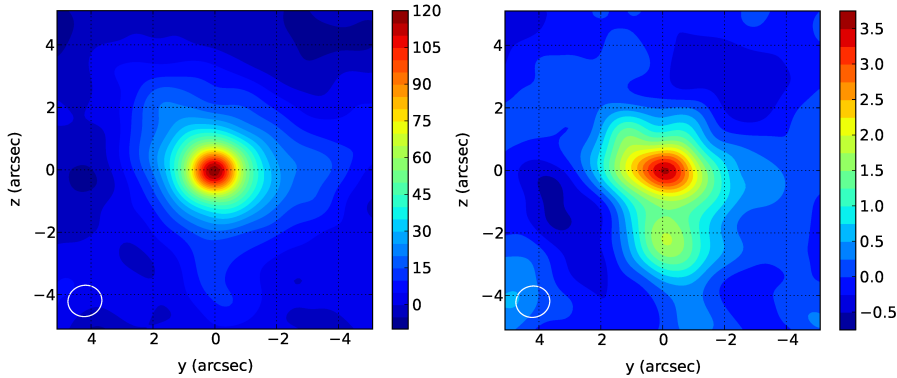


**Fig. 5** ALMA sky maps of the central region for Doppler velocities respectively larger (left) and smaller (right) than  $-14 \text{ km s}^{-1}$ . The color scales are in units of  $\text{Jy km s}^{-1} \text{ arcsec}^{-2}$ .

Figure 4 displays the sky maps of the detected fluxes over the whole fields of view. In the ACA data, a slight offset of the central star with respect to the origin of coordinates,  $0.4''$  north and  $1.3''$  west, has been corrected for in what follows.

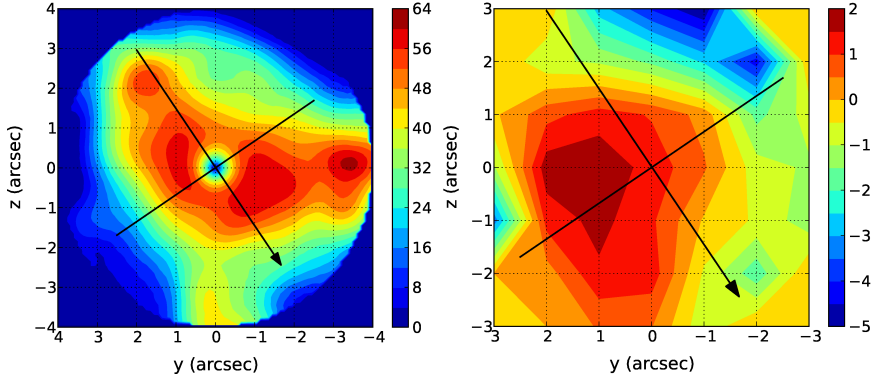
Figure 5 compares the ALMA sky maps of the central region for Doppler velocities respectively smaller and larger than  $-14 \text{ km s}^{-1}$ . The small excess observed in Figure 3 in the  $[-20, -14] \text{ km s}^{-1}$  interval (also present in single dish data) corresponds to short distances from the central star with a clear south enhancement at  $\sim 2''$ . Accordingly, in what follows, we restrict Doppler velocities to the interval spanning between  $-14$  and  $18 \text{ km s}^{-1}$  for ALMA data. The mean velocity of the selected sample of observations is  $V_x^* = 3.2 \text{ km s}^{-1}$ .

### 3 MORPHOLOGY AND KINEMATICS OF THE CSE AT SHORT DISTANCES ( $R < 4''$ )

Figure 6 (left) displays the sky maps of the measured flux (flux density integrated over Doppler velocities from  $-14 \text{ km s}^{-1}$  to  $18 \text{ km s}^{-1}$ ) multiplied by  $R$  for ALMA data and  $R < 4''$ . Multiplying by  $R$  would mean a uniform distribution for a  $1/r^2$  dependence of the emission ( $r$  being the space distance from the central star) and allows for better revealing inhomogeneities up to large distances. A clear enhancement is seen in the north-east/south-west direction, covering a broad angular range, and in the opposite direction, covering a narrower angular range. The broad enhancement is centred on  $\sim 40^\circ$  in the  $R < 2''$  interval and splits in two components when  $R$  increases, respectively centred on  $\sim 0^\circ$  and  $\sim 90^\circ$  in the  $2'' < R < 4''$  interval. This is also clearly seen in Figure 7 where the measured flux has been averaged over  $R < 2''$  and  $2'' < R < 4''$  separately in  $15^\circ$  wide  $\varphi$  bins.

Figure 6 (right) shows the sky map of the mean Doppler velocity, (averaged between  $-14 \text{ km s}^{-1}$  and  $18 \text{ km s}^{-1}$  and shifted by  $V_x^*$  to be centred on zero) for ALMA data and  $R < 3.5''$ ; large pixel sizes ( $1'' \times 1''$ ) are used in order to keep reasonable signal to noise values in each pixel. A clear asymmetry is revealed along the direction perpendicular to the line joining the central star to its companion, the south-east hemisphere being red-shifted and the north-west hemisphere blue-shifted. Again, this is

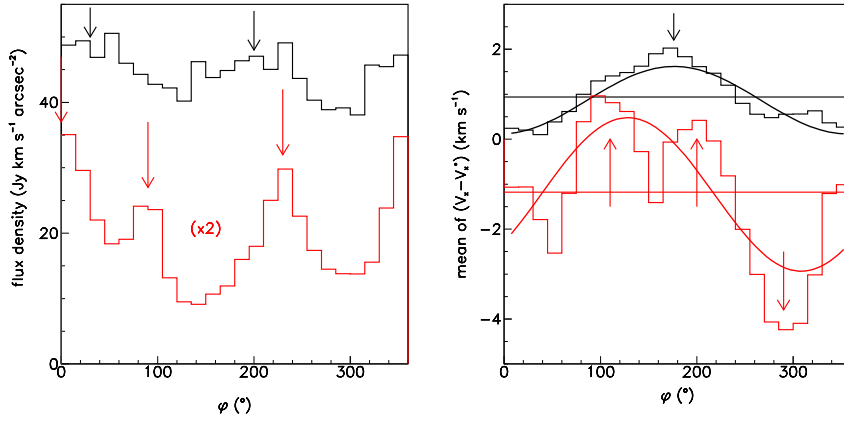
clearly seen in Figure 7 which displays the  $\varphi$ -distribution of the mean Doppler velocity averaged over  $R < 2''$  and over  $2'' < R < 3.5''$  separately and shifted by  $V_x^*$  to be centred on zero for ALMA data. Positive velocities are observed over a broad angular range in the south-east direction and negative velocities over a narrower angular range in the north-west direction. Sine wave fits of the form  $\langle V_x - V_x^* \rangle = V_0 + V_1 \cos(\varphi - \varphi_0)$  give  $V_0 = 0.87 \text{ km s}^{-1}$ ,  $V_1 = 0.75 \text{ km s}^{-1}$  and  $\varphi_0 = 176^\circ$  for  $R < 2''$  and  $V_0 = -1.23 \text{ km s}^{-1}$ ,  $V_1 = 1.71 \text{ km s}^{-1}$  and  $\varphi_0 = 128^\circ$  for  $2'' < R < 4''$ . However, the quality of the fit is poor in the latter case, the distribution being split in two maxima centred at  $\sim 100^\circ$  and  $\sim 190^\circ$  respectively.



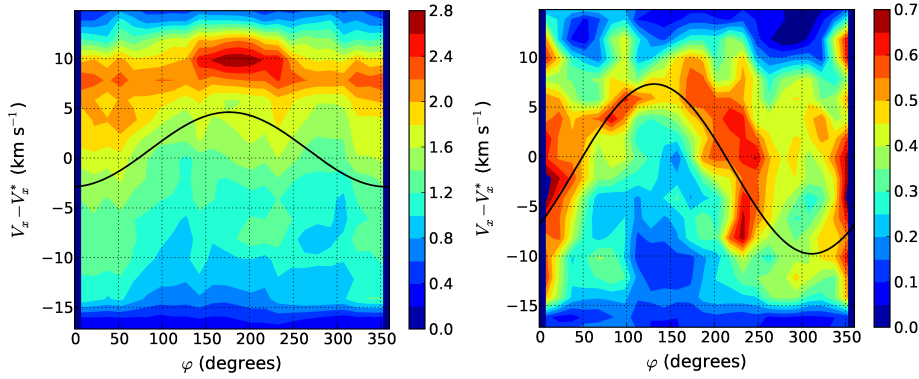
**Fig. 6** Left: sky map of the measured flux (flux density integrated over Doppler velocity from  $-14 \text{ km s}^{-1}$  to  $18 \text{ km s}^{-1}$ ) multiplied by  $R$  for ALMA data and  $R < 4''$ . Right: sky map of the mean Doppler velocity (averaged between  $-14 \text{ km s}^{-1}$  and  $18 \text{ km s}^{-1}$  and shifted by  $V_x^*$  to be centred on zero) for ALMA data and  $R < 3.5''$ ; large pixel sizes ( $1'' \times 1''$ ) are used in order to keep reasonable signal to noise values in each pixel. The line joining the central star to its companion is shown as a black arrow and the other black line is perpendicular to it. The colour scales are in  $\text{Jy km s}^{-1} \text{ arcsec}^{-1}$  and  $\text{km s}^{-1}$  respectively.

Figure 8 shows position-velocity diagrams in the  $V_x$  vs  $\varphi$  plane for ALMA data averaged over  $R < 2''$  and over  $2'' < R < 4''$  separately. What we call here a position-velocity diagram is different from what is normally meant by this term in the literature, namely a plot of the Doppler velocity as a function of a cut in the sky plane containing the source. However, it carries information of a similar nature and is particularly relevant when the radial dependence of the Doppler velocity is not too strong. As previously,  $V_x$  has been shifted by  $V_x^*$  to be centred on zero. The sine wave fits displayed on Figure 7 (right) are shown in Figure 8 with amplitudes multiplied by 5. In the first case, the maxima of emission correspond approximately to the extrema of velocity while in the second case they are in approximate quadrature with the extrema of velocity. Qualitatively, the situation can be summarized as follows: when scanning across the  $R < 4''$  interval, one evolves from a morphology elongated along the east/west direction with a velocity gradient directed along this same direction to a morphology elongated along the north-east/south-west direction (with a broad enhancement south-west and a narrow enhancement north-east) and a velocity gradient directed along the perpendicular to it. Moreover, the  $R < 2''$  region is red-shifted with respect to the  $2'' < R < 4''$  region by  $\sim 2.1 \text{ km s}^{-1}$ .

Figure 9 (left) shows the  $R$  distribution of the flux averaged over  $\varphi$  for ALMA data. An exponential fit of the form  $A_0 e^{-R/R_0}$  for  $R < 3''$  gives  $A_0 = 4.18 \text{ Jy km s}^{-1} \text{ arcsec}^{-2}$  and  $R_0 = 1.08''$ . The inhomogeneities apparent in the left panel of Figure 6, where the flux is multiplied by  $R$ , are too small to be visible. The drop beyond  $4''$  is the effect of the short spacing problem. Also shown in Figure 9 (right) is the dependence on  $R$  of  $\langle V_x - V_x^* \rangle$ . It decreases rapidly when  $R$  exceeds  $\sim 1.5''$ .



**Fig. 7** Left panel:  $\varphi$ -distribution of the measured flux for ALMA data and  $R < 2''$  (black) and  $2'' < R < 4''$  (red, multiplied by 2). The arrows indicate approximate locations of the observed enhancements ( $30^\circ$  and  $200^\circ$  in the first case,  $0^\circ$ ,  $90^\circ$  and  $230^\circ$  in the second). Right panel:  $\varphi$ -distribution of the mean Doppler velocity averaged over  $R < 2''$  (black) or over  $2'' < R < 4''$  (red) and over  $-14 < V_x < 18 \text{ km s}^{-1}$  (shifted by  $V_x^*$  to be centred on zero) for ALMA data. The arrows indicate approximate locations of the centres of the observed velocity enhancements,  $176^\circ$  in the first case,  $110^\circ$ ,  $200^\circ$  and  $290^\circ$  in the second). The horizontal lines indicate the mean values of  $\langle V_x - V_x^* \rangle$  in each of the two  $R$  intervals, respectively  $0.9$  and  $-1.2 \text{ km s}^{-1}$ .



**Fig. 8** Position velocity diagrams averaged over  $R < 2''$  (left panel) and over  $2'' < R < 4''$  (right panel). The ordinate is the Doppler velocity shifted by  $V_x^*$  to be centred on zero. The abscissa is the position angle in degrees measured clockwise from west. The sine waves are the fits displayed in Figure 7 (right) with amplitudes multiplied by 5.

Figure 10 illustrates the evolution of the direction of elongation of the emission and of the wind asymmetry when  $R$  increases. Here, directions of elongation are defined as the values of angle  $\varphi_0$  that maximize the mean values of  $\cos^2(\varphi - \varphi_0)$  and  $(V_x - V_x^*) \cos(\varphi - \varphi_0)$  respectively, weighted by the

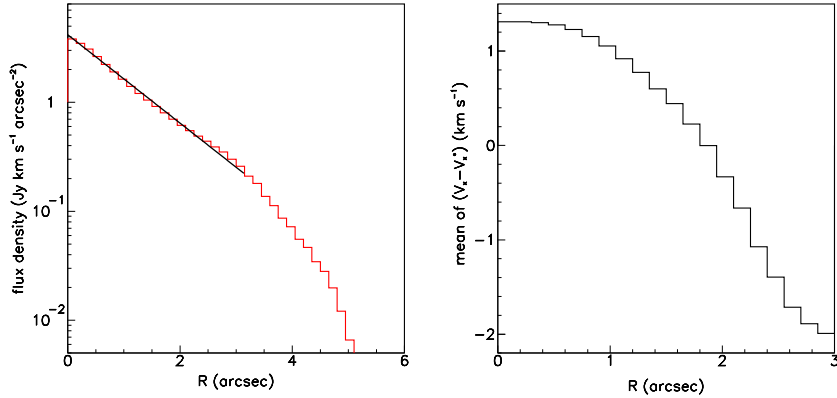


**Fig. 9** Left:  $R$ -distribution of the flux averaged over  $\varphi$  for ALMA data; the line is an exponential fit of the form  $4.18e^{-R/1.08''}$ . Right: dependence on  $R$  of the mean Doppler velocity, shifted by  $V_x^*$  to be centred on zero.

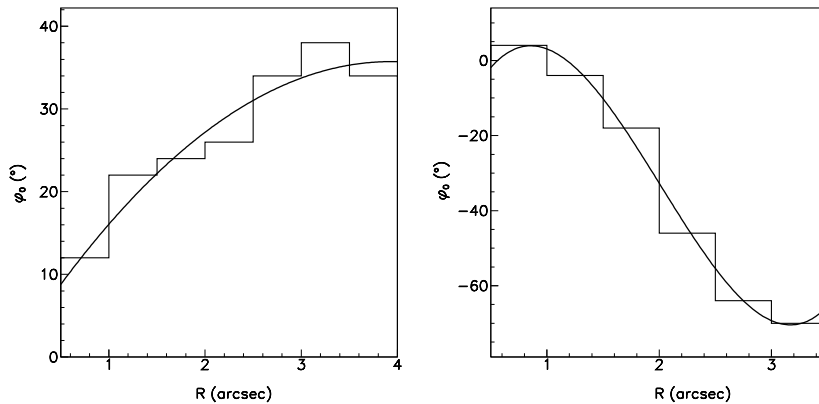


**Fig. 10** Left:  $R$ -distribution of the direction of the flux maximal elongation. Right:  $R$ -distribution of the direction of maximal velocity asymmetry. The curves are polynomial fits to guide the eye.

flux in each bin of  $R$  ( $0.5''$  wide). Here,  $V_x^*$  has been corrected to be the mean value of  $V_x$  in the relevant  $R$ -bin. They show very clearly the evolution of the flux maximal elongation from  $\sim 10^\circ$  above west to  $\sim 10^\circ$  below north-west and that of the maximal velocity asymmetry from west to  $\sim 20^\circ$  above north-west.

#### 4 MORPHOLOGY AND KINEMATICS OF THE CSE AT LARGE DISTANCES

The dusty CSE of W Aql is known to extend up to large distances, typically  $50''$  east and  $70''$  west, contained within an envelope described as a spiral by Mayer et al. (2013). From Mamon et al. (1988) we obtain an effective UV dissociation distance for CO molecules  $r_{1/2} \sim 1.5 \cdot 10^{17}$  cm, meaning  $\sim 10^4$  AU



or  $\sim 25''$ . The  $\varphi$ -distribution of the flux measured with the compact ACA array is displayed in Figure 11 for three  $R$  intervals,  $5''$  to  $10''$ ,  $10''$  to  $15''$  and  $15''$  to  $20''$ . They show clear enhancements in the western half-plane for  $5'' < R < 10''$ , joining smoothly with the enhancements observed in Figure 6 (left) for  $R < 4''$ , and at  $\pm 60^\circ$  from east for  $15'' < R < 20''$ , joining smoothly with the eastern enhancement observed by Mayer et al. (2013) for  $R > 20''$  (Figure 12 left).

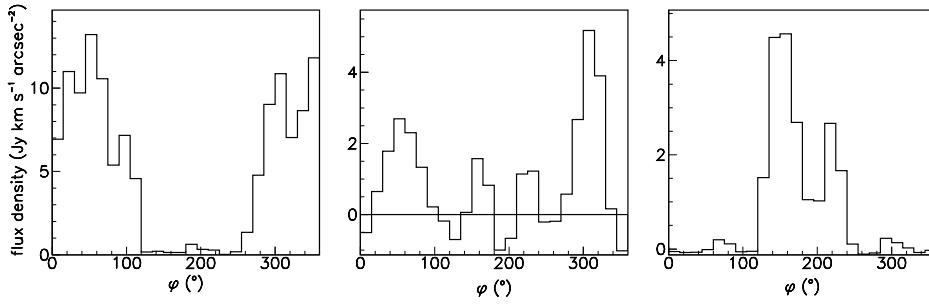


**Fig. 11** Distribution on  $\varphi$  of the flux measured with the compact ACA array, averaged over  $5'' < R < 10''$  (left),  $10'' < R < 15''$  (centre) and  $15'' < R < 20''$  (right).

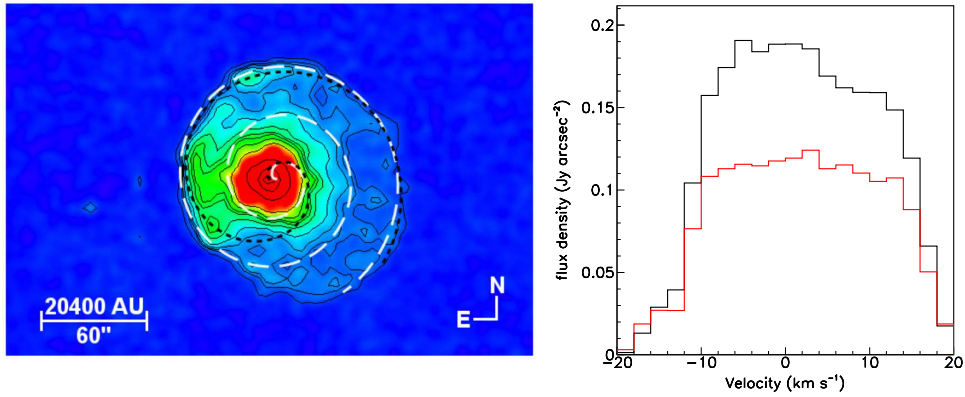


**Fig. 12** Left: large scale environment of W Aql observed by Mayer et al. (2013) at  $70 \mu\text{m}$  from Herschel/PACS. Right: velocity spectra averaged over the enhancements displayed in Figure 11:  $5'' < R < 10''$  and  $|\varphi| < \pi/2$  (black) and  $15'' < R < 20''$  and  $|\varphi - \pi| < \pi/3$  (red).

Figure 12 (right) displays the Doppler velocity distributions measured over each of these enhancements; they do not show any particular feature. Their mean velocities are  $1.8 \text{ km s}^{-1}$  and  $2.0 \text{ km s}^{-1}$  compared with  $V_x^* = 3.2 \text{ km s}^{-1}$  obtained at small distances from the central star for ALMA data. The present data do not allow for drawing a more detailed picture of the CSE at large distances from the star.

## 5 DISCUSSION AND SUMMARY

The analyses of the preceding sections show clearly that longer observation times, preferably including lines associated with several CO excitations, are needed in order to reach a reliable and detailed understanding of the morphology and kinematics of the CSE of W Aql. Yet, some qualitative but important results have been obtained that bring significant new information at the same time as they raise new questions.

The important slope of the line profile in the central region, of the order of 2% per  $\text{km s}^{-1}$ , is a surprising observation as is the rapid decrease of  $\langle V_x \rangle$  with  $R$  when  $R$  exceeds  $\sim 2''$ . This may be an effect of optical thickness, which is expected to affect more strongly small values of  $R$ , therefore to increase the measured value of the apparent mean Doppler velocity at small values of  $R$ . If such is the case, it raises the question of the importance of optical thickness on the interpretation of the results presented in the preceding sections. To a first approximation, one would expect the  $\varphi$ -dependence of the measured quantities at fixed values of  $R$  not to be much affected.

The measurement of the star velocity in the local standard of rest (LSR) frame is made difficult by the variability of the star and its interaction with its companion. Mayer et al. (2013) have presented a detailed analysis of available data and have concluded that the space velocity of W Aql is  $V_{LSR} = 21.6 \pm 4.1 \text{ km s}^{-1}$  with a position angle of  $38^\circ$  and an inclination of  $-17^\circ$  with respect to the line of sight. Our value of  $V_x^*$ ,  $3.2 \text{ km s}^{-1}$ , would therefore suggest  $-25.5 + 3.2 = -22.3 \text{ km s}^{-1}$  compared with  $-21.6 \cos(17^\circ) = -20.8 \text{ km s}^{-1}$  and with  $-23.0 \text{ km s}^{-1}$  used by Danilovich et al. (2014), namely a good agreement given the measurement uncertainties, in particular the dependence on  $R$ , probably the effect of optical thickness.

The large mass loss rate of W Aql has significantly shaped its CSE away from spherical. The complex structure of the wind velocity field suggests that different regimes have dominated over time. The approximate coincidence between the projected position of the companion and the direction of the dominant winds may be accidental: to decide on this important issue requires more detailed information than available here.

A velocity gradient along a direction projecting at position angle  $\varphi_0$  in the plane of the sky may be interpreted, among others, as an expansion along an axis projecting at position angle  $\varphi_0$  or as a rotation about an axis projecting at position angle  $\varphi_0 + \pi/2$ . In both cases the axis should have a significant inclination with respect to the line of sight for the gradient to be observed. At short distances ( $R < 4''$ ) the present data do not allow for choosing between these two interpretations, or possibly suggesting a different one.

When new ALMA data will become available, the understanding of the properties of the CSE of W Aql will require the use of a model taking due account of radiative transfer in order to properly describe the effect of absorption at short projected distances from the central star, as the measured line profile, and its dependence over  $R$ , suggest significant optical thickness in this central region. For the model parameters, in particular the temperature, to be well constrained by observations, it will be necessary to observe emission from at least two different rotational lines of the CO molecule.

The presence of spikes at the extremities of the Doppler velocity distribution, for  $|V_x|$  between  $\sim 14$  and  $\sim 20 \text{ km s}^{-1}$ , is not understood. While the blue-shifted spike is enhanced at small distances south of the central star (Figure 5), no similar enhancement can be revealed for the red-shifted spike.

Finally, the observation of CO(3-2) emission at large distances from the central star using the compact ACA array is consistent with the results obtained earlier from dust emission in the far infrared but the present data are not sufficient to reveal details such as a possible spiral structure as observed by Mayer et al. (2013).

## ACKNOWLEDGEMENTS

We are indebted and very grateful to the ALMA partnership, who are making their data available to the public after a one year period of exclusive property, an initiative that means invaluable support and encouragement for Vietnamese astrophysics. We particularly acknowledge friendly and patient support

from the staff of the ALMA Helpdesk. We express our deep gratitude to Professors Nguyen Quang Rieu and Thibaut Le Bertre for having introduced us to radio astronomy and to the physics of evolved stars. Financial support is acknowledged from the Vietnam National Satellite Centre (VNASC/VAST), the NAFOSTED funding agency, the World Laboratory, the Odon Vallet Foundation and the Rencontres du Viet Nam.

## References

- Alfonso-Garzón, J., Domingo, A., Mas-Hesse, J. M. & Giménez, A., 2012, *A&A*, 548, A79
- Castro-Carrizo, A., Quintana-Lacaci, G., Neri, R., et al., 2010, *A&A*, 523, A59
- Danilovich, T., Bergman, P., Justtanont, K., et al., 2014, *A&A*, 569 A, 76
- Danilovich, T., Oloffson, G., Black, J. H., et al., 2015, *A&A*, 574A, 23
- De Beck, E., Decin, L., de Koter, A., et al., 2010, *A&A*, 523, A18
- Feast, M. W. & Whitelock, P. A., 2000, *MNRAS*, 317, 460
- Guandalini, R. & Busso, M., 2008, *A&A*, 488, 675
- Keenan, P. C. & Boeshaar, P. C., 1980, *ApJS*, 43, 379
- Knapp, G. R., Young, K., Lee, E., & Jorissen, A., 1998, *ApJS*, 117, 209
- Kukarkin, B. V., Kholopov, P. N., Pskovsky, Y. P., et al., 1971, in *General Catalogue of Variable Stars*, 3rd ed. (1971)
- Loup, C., Forveille, T., Omont, A. & Paul, J. F., 1993, *A&A*, 99, 291
- Mamon, G. A., Glassgold, A. E. & Huggins, P. J., 1988, *AJ*, 328, 797
- Mayer, A., Jorissen, A., Kerschbaum, F., et al., 2013, *A&A* 549, A69
- Nyman, L.-Å., Booth, R. S., Carlström, U., et al., 1992, *A&A*, 93, 121
- Ramstedt, S., Schöier, F. L., & Olofsson, H., 2009, *A&A*, 499, 515
- Ramstedt, S., et al., 2011, *A&A* 531, A148
- Ramstedt, S. & Olofsson, H., 2014, *A&A* 566, A145
- Sloan, G. C., & Price, S. D., 1998, *ApJS*, 119, 141
- Tatebe, K., Chandler, A.A, Hale, D. D. S. & Townes, C. H., 2006, *ApJ*, 652, 66
- Wallerstein, G., Balick, B., Alcolea, J., Bujarrabal, V. & Vanture, A. D., 2011, *A&A*, 535, A101
- Whitelock, P., Menzies, J., Feast, M., et al., 1994, *MNRAS*, 267, 711
- Whitelock, P.A., Feast, M. W. & van Leeuwen, F., 2008, *MNRAS*, 386, 313